Vertical wind shear on Jupiter from Cassini images

Liming Li,[1] Andrew P. Ingersoll,[1] Ashwin R. Vasavada,[2] Amy A. Simon-Miller,[3] Anthony D. Del Genio,[4] Shawn P. Ewald,[1] Carolyn C. Porco,[5] and Robert A. West[2]

Received 12 August 2005; revised 3 January 2006; accepted 12 January 2006; published 14 April 2006.

[1] Multifilter images of Jupiter acquired by the Cassini Imaging Science Subsystem (ISS) are used to derive zonal winds at altitudes above and below the visible cloud deck. Small features unique to the ultraviolet images of ISS are tracked to get the systematic high-altitude zonal winds. Comparison between the zonal winds from ultraviolet images and the vertical profile of zonal winds from the Cassini Composite Infrared Spectrometer (CIRS) shows that the zonal winds from the ultraviolet images are from a pressure level that is ~0.2 scale heights higher than the pressure level of the zonal winds from continuum-band images. Deeper zonal winds at different latitudes of the equatorial region are measured by tracking cloud features observed within hot spots on continuum-band images. The deeper zonal winds in this study extend the measurement of the Galileo probe to different latitudes of the equatorial region. Comparison between the Galileo probe and this study suggests that these fast-moving clouds within hot spots are deeper than 3 bars and are therefore probably water clouds.

Citation: Li, L., A. P. Ingersoll, A. R. Vasavada, A. A. Simon-Miller, A. D. Del Genio, S. P. Ewald, C. C. Porco, and R. A. West (2006), Vertical wind shear on Jupiter from Cassini images, *J. Geophys. Res.*, *111*, E04004, doi:10.1029/2005JE002556.

1. Introduction

[2] The vertical structure of zonal winds on Jupiter is critical for understanding the origin of the global-scale circulation on the giant planet [*Barcilon and Gierasch*, 1970; *Gierasch*, 1976; *Ingersoll and Pollard*, 1982]. Most measurements of zonal winds from ground-based telescopes, Voyager, HST, Galileo, and Cassini are limited to motions within the visible cloud deck and are made by tracking clouds in sequences of images taken at time intervals of ~1 hour to ~1 day [*Garcia-Melendo and Sanchez-Lavega*, 2001; *Ingersoll et al.*, 1979, 1981; *Limaye*, 1986, 1989; *Porco et al.*, 2003; *Rogers*, 1995; *Simon*, 1999; *Smith*, 1976; *Vasavada et al.*, 1998]. In this paper, the visible cloud deck refers to the features seen at visible wavelengths in broadband continuum filters. Although the chemical components and pressure levels are uncertain [*Banfield et al.*, 1998; *Irwin et al.*, 2005], the principal cloud is probably ammonia (NH_3) at a pressure level around 0.7 bar, in agreement with the classical cloud scheme from thermodynamic modeling [*Atreya et al.*, 1997].

[3] The Galileo Doppler Wind Experiment (DWE) is the only measurement of the winds below the visible cloud deck [*Atkinson et al.*, 1998]. High-altitude zonal winds decaying with altitude above the visible cloud deck are suggested by the Voyager Infrared Interferometer Spectrometer (IRIS) thermal measurements and the thermal wind equation [*Gierasch et al.*, 1986]. Several attempts to detect vertical wind shear by tracking clouds in images at different wavelengths were inconclusive [*Simon*, 1999; *Garcia-Melendo and Sanchez-Lavega*, 2001]. *Banfield et al.* [1996] measured high-altitude zonal winds at limited sites in the southern hemisphere of Jupiter by studying the impact debris from Comet Shoemaker-Levy 9. *Vincent et al.* [2000] performed measurements of the zonal motions in Jupiter's high-altitude atmosphere by tracking selected features on the HST ultraviolet images, but the measurements are limited by poor limb-darkening correction of images in low latitudes and irregular intervals between images ranging from 10 to 70 hours. Here we present the Cassini imaging data that yield the zonal winds above and below the level of the visible cloud deck.

[4] The Cassini flyby of Jupiter produced a wealth of scientific data. The wide spectral range of the Imaging Science Subsystem (ISS), from the ultraviolet (UV) into the near-infrared (near-IR), can discriminate Jupiter's multilevel clouds and hazes [*Porco et al.*, 2003]. Multifilter ISS images taken at different times make it possible to measure zonal winds at different pressure levels by tracking multilevel clouds and hazes. During the encounter, the Cassini Composite Infrared Spectrometer (CIRS) returned spectra of the Jovian atmosphere from 10–1400 cm^{-1} (1000–7 μm) at a programmable spectral resolution of 0.5 to 15 cm^{-1}. The vertical profile of zonal winds above the visible cloud deck has been estimated by combining the temperature maps constructed from these spectra with the thermal wind equation [*Flasar et al.*, 2004; *Simon-Miller et al.*, 2006].

[1]Division of Geological and Planetary Sciences, California Institute of Technology, Pasadena, California, USA.
[2]Jet Propulsion Laboratory, California Institute of Technology, Pasadena, California, USA.
[3]NASA Goddard Space Flight Center, Greenbelt, Maryland, USA.
[4]NASA Goddard Institute for Space Studies, New York, New York, USA.
[5]CICLOPS/Space Science Institute, Boulder, Colorado, USA.

0148-0227/06/2005JE002556$09.00

Table 1. Information for the Cassini ISS Nine Filters[a]

Filter	λ_{center}, nm	$\lambda_{effetive}$, nm	Observation Times	Pressure (τ = 1)
UV1	258	264	1 Oct to 14 Nov	350 mbar
BL1	451	455	1 Oct to 14 Nov	4.5 bar
GRN	568	569	1 Oct to 14 Nov	10 bar
MTi	619	619	1 Oct to 14 Nov	10 bar
CB1	619	619	1 Oct to 14 Nov	>10 bar
MT2	727	727	1 Oct to 14 Nov	4 bar
CB2	750	750	1 Oct to 9 Dec, 11–13 Dec	>20 bar
MT3	889	889	1 Oct to 14 Nov	600 mbar
CB3	938	938	1 Oct to 14 Nov	>50 bar

[a]Filters column gives names of different filters; λ_{center} and $\lambda_{effetive}$ are center and effective wavelengths of the different filters. The effective wavelengths are computed using the full system transmission function convolved with a solar spectrum [*Porco et al.*, 2005], which are more relevant to the optical characteristics of filters. Observation times are the observation times for different filters. Pressure is the effective pressure level, which is defined as optical depth τ = 1 in the absence of cloud opacity. The effective pressure levels are estimated by taking account of Rayleigh scattering and methane-absorption for these ultraviolet, visible, and near-infrared filters [*West et al.*, 2004].

The simultaneous observations of the ISS and the CIRS offer an unprecedented opportunity to compare estimates of the zonal winds above the visible cloud deck from these two subsystems of Cassini.

[5] The Galileo probe entered into a 5-micron hot spot, which is a hole in the visible cloud deck [*Young*, 2003]. The wind velocity was ~100 m/s at the level of the visible cloud deck, which agrees with the cloud-tracked winds for the latitude (7.4°N planetographic) at which the probe entered. From there the winds increased to 180 m/s at the 4- to 5-bar level. After that, the winds stayed constant at 170–180 m/s down to the 21-bar level [*Atkinson et al.*, 1998]. Seen from outside the atmosphere, the hot spots appear to move with most of the other visible cloud features in Jupiter's bright equatorial band (7°N–10°N) [*Vasavada et al.*, 1998]. If there are clouds at deeper levels, it should be possible to see them through holes in the upper clouds; they should appear as small clouds within the hot spots. We have examined some of the hot spots in the continuum filter (CB2), where the gases are transparent and the only significant opacity above 10 bars is due to clouds [*Banfield et al.*, 1998], to check the possibility of measuring the deep wind by tracking these deep clouds through the hot spots.

2. Description of Image Sets

[6] The ISS images analyzed in section 3 consist of narrow-angle camera (NAC) images in nine filters (UV1,

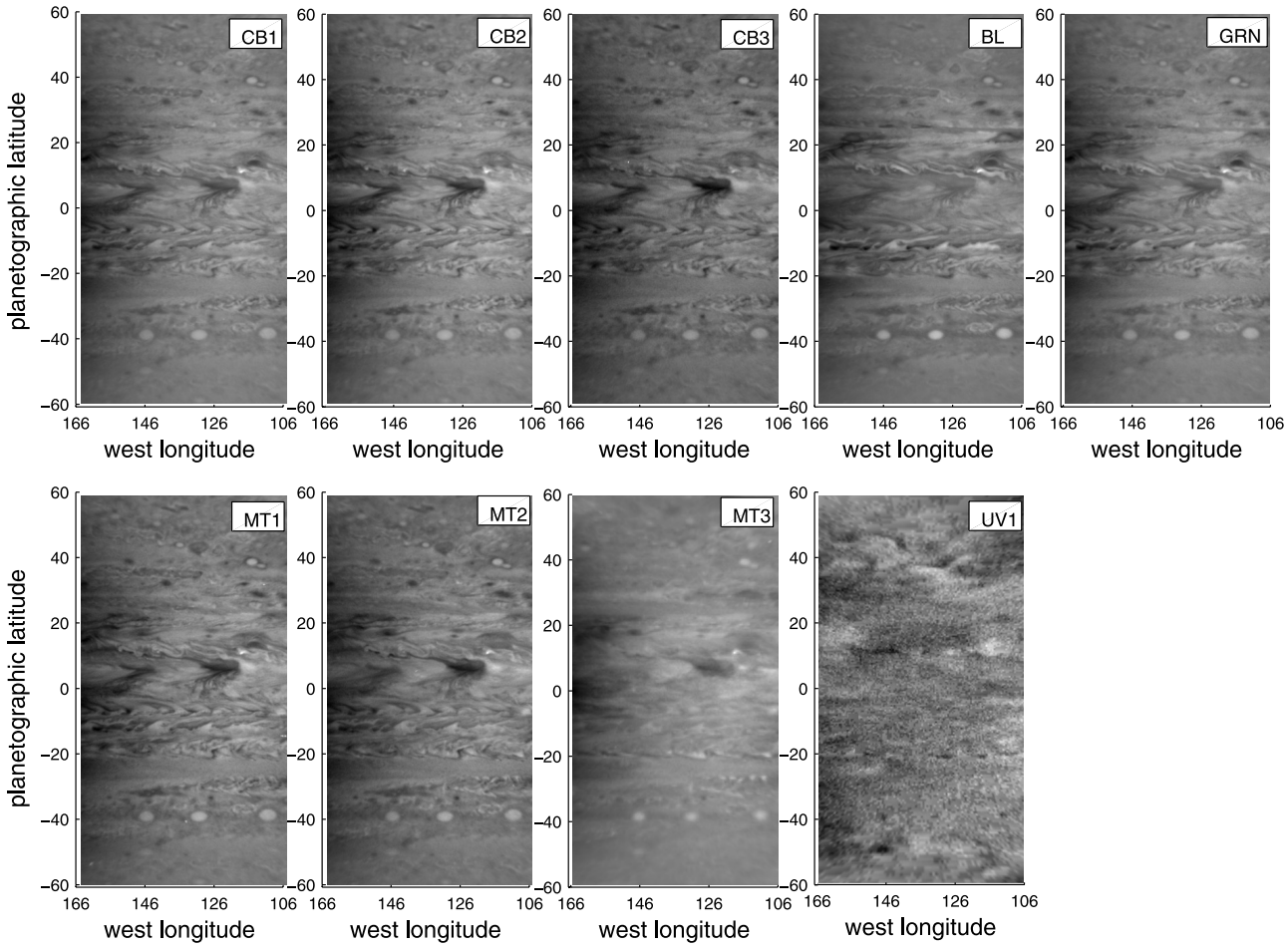

Figure 1. Map-projected images of the same area in nine filters. The images were taken at intervals of 40 s, which makes them virtually simultaneous. The mean value of every constant-latitude line in the MT3 and UV1 images is removed so that the feature contrast covered by the equatorial haze in MT3 and UV1 can be seen.

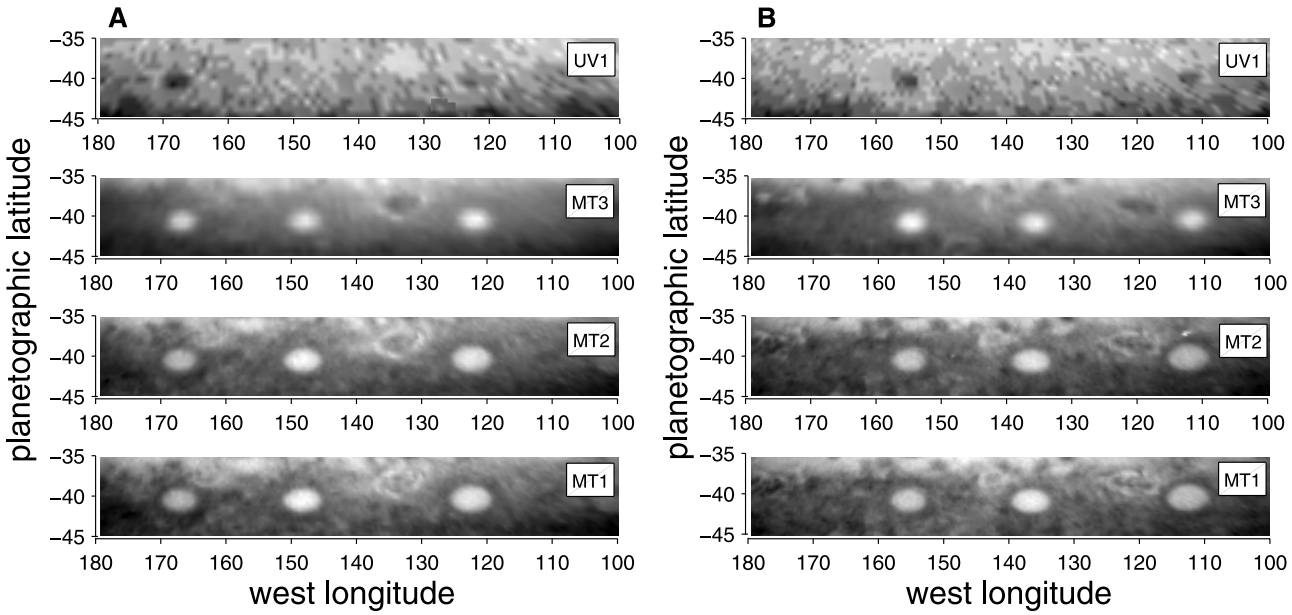

Figure 2. Features visible in UV1, MT3, MT2, and MT1 images at two different times. For Figures 2a and 2b the UV1, MT3, MT2 and MT1 are near-simultaneous images separated by 40 or 80 s. The time separation between Figures 2a and 2b is 15 days. The mean value of every constant-latitude line in the UV1 images is removed to make the feature contrast clear.

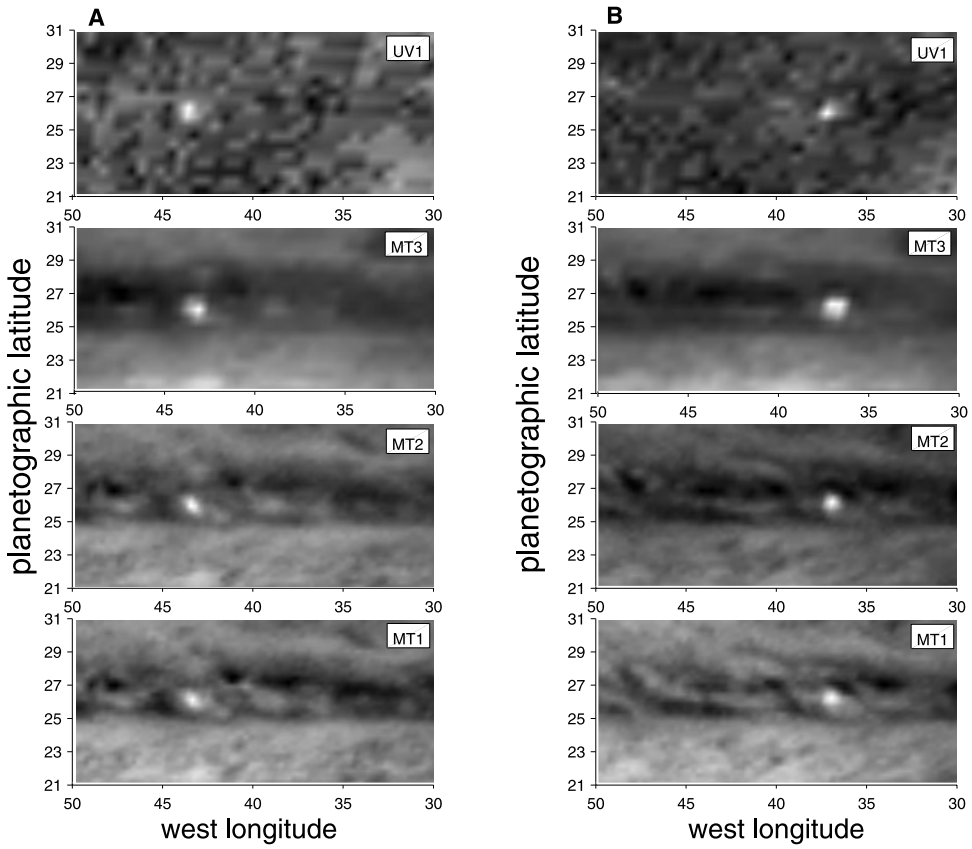

Figure 3. One moist convective storm visible in UV1, MT3, MT2, and MT1 images at two different times. For Figures 3a and 3b the UV1, MT3, MT2 and MT1 are near-simultaneous images separated by 40 or 80 s. The time separation between Figures 3a and 3b is 20 hours. The mean value of every constant-latitude line in the MT3 and UV1 images is removed to make the feature contrast clear.

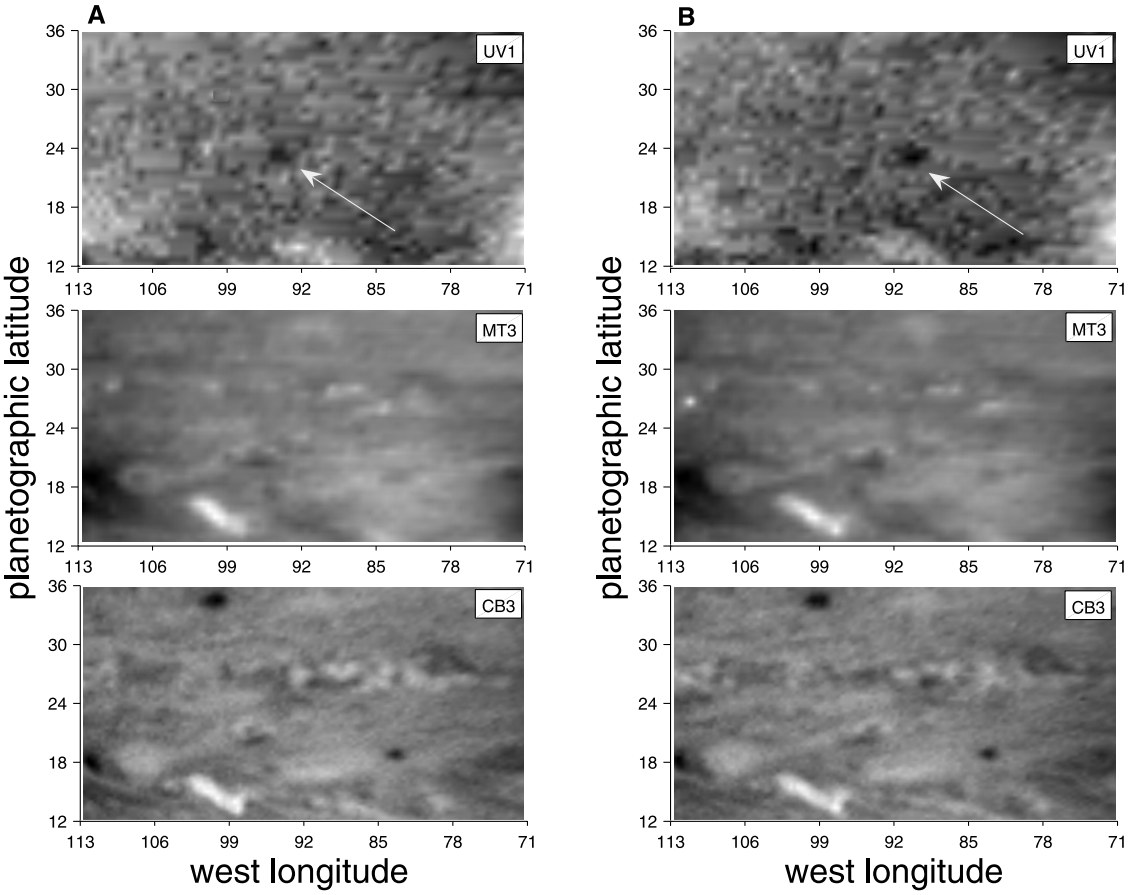

Figure 4. Feature visible in UV1 image and invisible in MT3 and CB3 images at two different times. For Figures 4a and 4b the UV1, MT3, and CB3 are near-simultaneous images separated by 40 s. The time separation between Figures 4a and 4b is 20 hours. The mean value of every constant-latitude line in the MT3 and UV1 images is removed to make the feature contrast clear.

BL1, GRN, MT1, CB1, MT2, CB2, MT3, and CB3) acquired over a 45-day period (1 October to 14 November 2000) [*Porco et al.*, 2004]. The ISS images analyzed in section 4 include additional CB2 images after the 45-day period (15 November to 9 December 2000) and 1 × 2 North-South mosaics acquired every 63 min in a separate image set (11–13 December 2000). Information including center wavelength, observation time, and effective pressure level (optical depth $\tau = 1$ in the absence of cloud opacity) for the nine filters are shown in Table 1. The methane filters MT1, MT2, and MT3 are centered on weak, medium, and strong absorption bands, respectively. The continuum filters CB1, CB2, and CB3 are paired to the corresponding MT filters, but are at wavelengths where the atmospheric gases are relatively transparent. Global mosaics of the same filter are separated by either 10 or 20 hours. Mosaics of different filters are taken 40 s apart so that each nine-filter set is near simultaneous.

[7] Each image was navigated by fitting (in the image plane) the observed planetary limb to its predicted location. This procedure locates the limb to a precision much less than one pixel, but may introduce systematic errors due to imprecise knowledge of the altitude of limb-defining opacity. However, wind measurements are performed on images that were navigated using the same portion of the planetary limb, resulting in systematic errors that occur in the same direction and that are partially mitigated by a relative wind measurement. The spatial resolution in the image plane of the October–November data ranged from 506 to 262 km/pixel, while that in the December data is ~120 km/pixel. The full width at half maximum (FWHM) of the point spread function (PSF) of the NAC through the clear filters is 1.3 pixels. At these resolutions, a one-pixel uncertainty in the navigation of the raw images would result in wind speed errors of 3–14 m/s at the equator, when measured using images separated by 10 hours. Navigation error can be estimated directly when the images are mapped and combined into global mosaics. Inspection of the overlap regions reveals errors of less than a few map pixels, often less than one map pixel (one map pixel is 0.1 degree, or ~125 km at the equator), giving an error of less than 3 m/s in wind speed. Radiometric calibration was performed using the CISSCAL software developed by the Cassini ISS Team [*Porco et al.*, 2004]. The map projection is simple cylindrical (rectangular) with equal increments of planetocentric latitude and longitude. Every map is 1801 × 1801 pixels (180 degrees of latitude and longitude at 0.1 degree per pixel). In this paper, we use planetographic latitude and west longitude defined in System III [*Riddle and Warwick*, 1976].

3. High-Altitude Winds

[8] Figure 1 shows an example of the near-simultaneous nine-filter maps. The same features show up in most of the

Table 2. Zonal Wind by Tracking Features Unique to UV1 Images[a]

Latitude Number (Graphic)	Wind, m/s	Error, m/s	Number
	Northern Hemisphere		
54.8	9.4	-	1
53.6	0.0	-	1
52.1	−8.9	-	1
50.7	−3.1	3.3	11
50.0	−2.1	4.0	22
49.1	−1.0	4.3	14
47.9	4.2	5.7	10
46.8	2.5	3.2	6
46.1	1.1	5.8	13
45.0	2.6	4.8	27
44.0	1.7	5.5	30
43.0	3.6	7.4	13
42.1	1.1	6.9	37
40.9	−0.2	6.5	60
40.1	−4.7	5.8	88
39.1	−4.7	6.8	65
38.0	−3.0	7.3	34
37.2	0.9	3.9	8
36.0	−1.7	7.4	43
35.1	10.7	11.5	8
34.0	8.1	11.6	18
33.0	3.5	12.2	35
32.0	−2.3	18.0	4
30.9	−9.2	13.1	10
30.0	−9.9	6.6	85
29.4	−0.9	12.9	9
28.3	32.5	-	1
27.0	32.4	5.4	3
26.2	60.8	17.1	8
25.2	95.1	-	1
23.7	111.5	8.4	30
23.3	108.6	6.7	64
22.2	72.3	19.7	3
20.9	57.1	19.0	2
19.7	27.0	12.2	11
19.1	9.2	10.0	32
18.3	3.0	7.2	5
17.1	6.2	8.2	4
15.9	3.6	8.2	17
15.0	5.0	11.8	15
13.9	16.3	6.6	9
13.0	27.0	11.4	24
12.0	30.2	10.0	29
11.0	47.1	13.8	20
10.2	49.7	9.8	13
9.3	71.9	6.8	2
7.9	82.5	3.4	2
6.9	79.6	6.0	9
6.1	76.3	7.7	4
4.2	79.5	-	1
1.1	81.7	11.2	6
	Southern Hemisphere		
−58.9	−1.3	6.9	3
−58.1	0.5	7.2	2
−57.4	−3.9	-	1
−54.8	−4.7	2.6	2
−54.0	6.0	6.4	21
−53.0	12.7	7.8	32
−52.0	10.0	6.3	22
−50.9	7.3	5.6	8
−50.1	5.1	6.8	19
−48.9	4.7	7.1	19
−48.0	−1.9	5.5	7
−47.0	11.6	8.8	7
−44.8	18.8	14.4	4
−43.2	15.6	-	1
−41.0	13.5	-	1
−39.9	4.8	6.6	10
−39.0	7.1	6.5	45
−38.4	11.8	6.3	2
−36.8	14.2	0.0	1
−35.9	23.0	0.0	1
−35.2	10.1	1.5	2
−33.0	0.0	-	1
−32.0	−2.8	5.9	19
−31.1	3.3	5.3	90
−27.5	28.0	-	1
−26.8	19.8	2.9	3
−26.3	18.9	3.2	2
−23.8	9.1	5.9	3
−22.9	-15.5	18.8	11
−22.2	−21.5	16.4	27
−21.1	−32.9	11.8	6
−20.0	−38.7	10.0	23
−19.3	−40.7	8.4	11
−18.0	−16.9	10.8	15
−17.1	−13.0	9.0	17
−16.5	−10.0	-	1
−13.8	20.3	-	1
−12.9	22.9	2.6	2
−12.2	10.2	3.4	2
−11.1	47.5	15.9	7
−10.0	63.7	16.7	11
−9.2	73.3	11.8	23
−7.9	61.9	3.7	4
−7.0	95.9	17.4	10
−6.0	86.8	14.8	18
−5.0	89.3	16.2	17
−4.2	77.4	12.4	22
−1.0	88.4	7.9	3
−.05	83.2	-	1

[a]The planetographic latitudes in the latitude column are average latitudes of the features tracked within the 1° latitude bin. Wind column gives the corresponding average zonal winds within the 1° latitude bin. Error column gives uncertainties calculated by the standard deviation of the multiple measurements within the 1° latitude bin. Dashed lines indicate that only one measurement was done within the corresponding latitude bin. Numbers column gives the number of measurements in the corresponding 1° latitude bin.

filters, indicating that one is viewing the same clouds at roughly the same altitudes in most of the images. The UV1 map differs the most from the others, suggesting that it is viewing features at a different altitude. Previous wind measurements trying to detect zonal winds at different altitudes [*Garcia-Melendo and Sanchez-Lavega*, 2001; *Simon*, 1999] probably track the same features appearing in different wavelength images so that no significant velocity differences between these different wavelength images are detected. Many features in the Cassini multifilter images behave the same way. Figure 2 shows an example where the same features appearing in different filter maps have the same velocities. Here we show four-filter maps (UV1, MT3, MT2, and MT1) with significantly different effective pressure levels (350 mbar for UV1, 600 mbar for MT3, 4 bar for MT2, and 10 bar for MT1) under cloud-free conditions. The two ovals existing in longitude 123° and 167° appear in the four filters of Figure 2, which suggests that the two ovals have large vertical structure. Furthermore, each of the two ovals keeps the same positions in the four filters even after 15 days (groups A and B of Figure 2 are separated by 15 days). It shows that the vertical shear of ambient zonal winds (if there is any) does not shift the vertical structure of

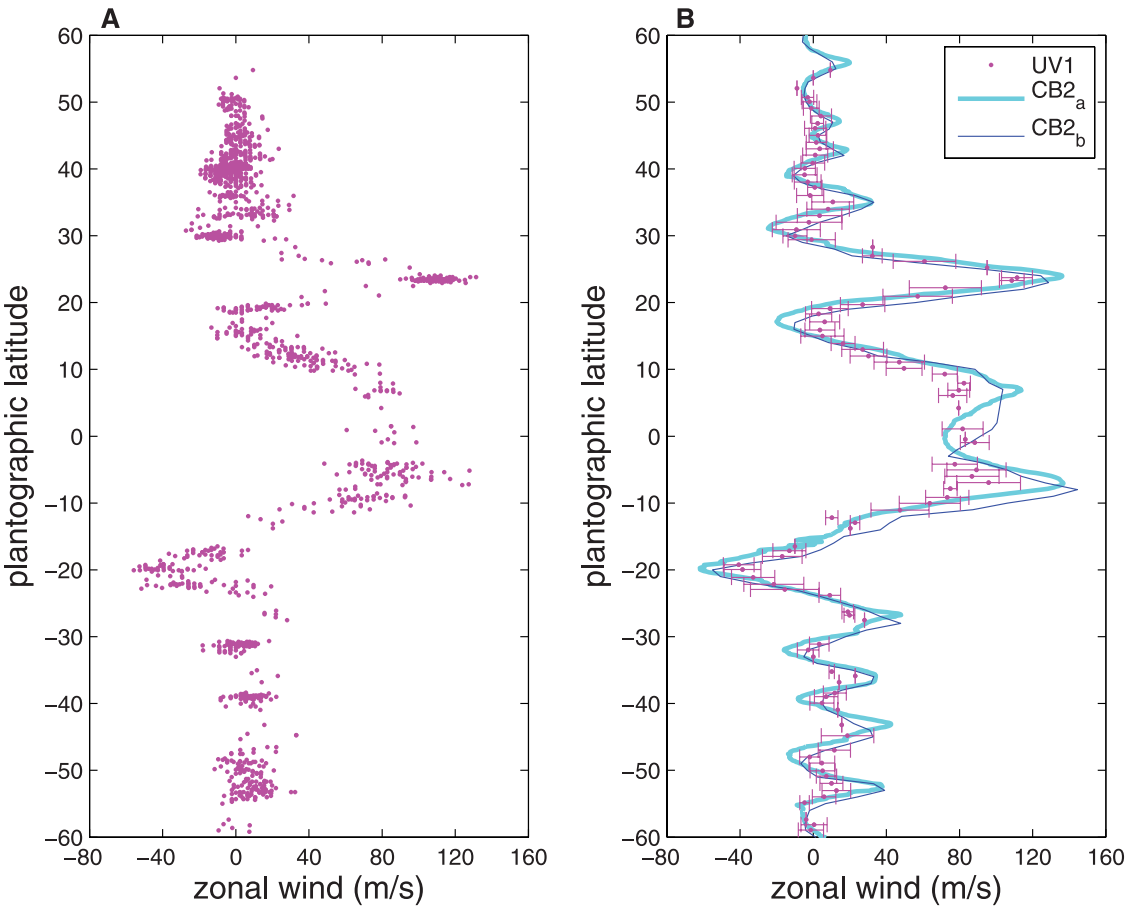

Figure 5. Measurements of zonal wind by tracking features unique to the UV1 images and comparison to the CB2 zonal wind profiles. (a) All 1529 measurements performed on the UV1 images. (b) Comparison of the average UV1 zonal winds and two zonal winds from CB2 images [*Porco et al.*, 2003; *Li et al.*, 2004]. Each dot in (**A**) represents a single measurement. Each dot in Figure 5b represents the average zonal wind of these measurements in Figure 5a within a 1° latitude bin. The $CB2_a$ zonal wind profile comes from automated correlation method utilizing 29 pairs of Cassini CB2 images separated by 10 hours [*Porco et al.*, 2003] and the $CB2_b$ comes from manually feature-tracking method utilizing CB2 images from 1 October to 9 December 2000 [*Li et al.*, 2004]. The uncertainties in Figure 5b are estimated by the standard deviation of the multiple measurements within the 1° latitude bins.

the two ovals, probably because the ovals are coherent in the vertical. In addition, the anticorrelation of brightness in UV1 and MT3 (dark in UV1 and bright in MT3) suggests that the ovals have UV-absorbing components at high altitude that appear dark relative to the Rayleigh scattering gas. These same components appear bright in MT3 relative to the methane absorbing gas. An exception to the anti-correlation between UV1 and MT3 is shown in Figure 3. The moist convective storm shown in Figure 3 has a bright appearance in both UV1 and MT3, which suggests that the cloud particles are bright in the UV and penetrate to higher altitude than the effective pressure level of UV1 ~350 mbar. The moist convective storm keeps the same position in the four filter images of each group A and B (separated by 20 hours), which also suggests that the vertical shear of the ambient zonal winds does not affect the vertical structure of the moist convective event.

[9] We selected small features unique to the UV1 filter images in order to track high-altitude winds. A sample of such features is shown in Figure 4. Columns A and B are two multifilter image sets separated by 20 hours. The dark feature sitting at latitude 24° in the UV1 image, which does not appear in the MT3 and CB3 images, suggests that this feature is high-altitude UV-absorbing haze. The feature has a velocity of 110 m/s, which is slower than the corresponding velocity, 130 m/s, in the CB2 filter at the same latitude. Figure 4 also shows that the dark feature changes shape during the 20-hour period. The rapidly varying characteristic of features in UV1 filter combined with lower feature contrast in the UV1 filter makes it difficult to measure zonal winds by an automated correlation method [*Limaye et al.*, 1982]. Therefore we manually track these features unique to the UV1 images to measure the high-altitude zonal winds. Features appearing in both UV1 images and other filter images are not included in this study. We increase the feature contrast of UV1 images by removing the mean value of every constant-latitude line of the UV1 images and utilizing the VICAR software developed by the Jet Propulsion Laboratory. Most of these features have sizes less than 4° in latitude and longitude,

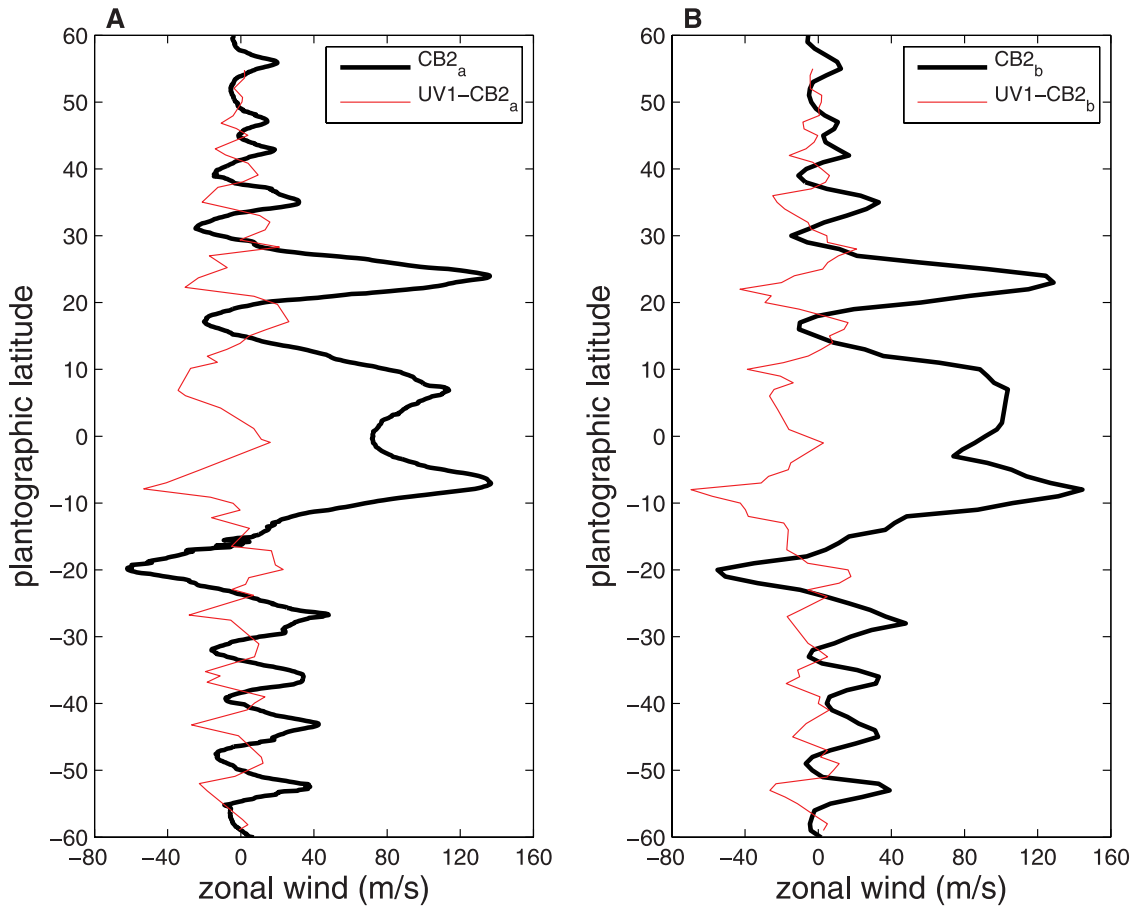

Figure 6. Differences between the UV1 zonal winds and the CB2 zonal winds. (a) Difference between the UV1 zonal winds and the $CB2_a$ zonal winds [*Porco et al.*, 2003]. (b) Difference between the UV1 zonal winds and the $CB2_b$ zonal winds [*Li et al.*, 2004].

which are equivalent to 4000 km at latitude 30° and are much larger than the spatial resolution, which is 500–250 km/pixel during the observing epoch (1 October to 14 November 2000). Some features are bright relative to their surroundings and others are dark. The features we tracked have different shapes (ovals, elongated, and irregular). All the above characteristics of these features unique to UV1 images are independent of latitude.

[10] Table 2 summarizes our measurements of high-altitude zonal winds by tracking these small features unique to the UV1 images. The uncertainties of zonal winds (columns 3 and 7 of Table 2), which are estimated by the standard deviation of the multiple measurements, vary around 10 m/s with the maximal value less than 20 m/s. In Figure 5a we present all 1529 measurements of high-altitude zonal winds by tracking small features unique to the UV1 images. The solid curves in Figure 5b are the zonal wind profiles derived from the continuum filter CB2 images, with the heavy solid line coming from the automatic correlation method [*Porco et al.*, 2003] and the light solid line coming from the manual tracking method [*Li et al.*, 2004]. The points with error bars in Figure 5b are averages in 1° latitude bins of individual velocity vectors shown in Figure 5a. The error bars are estimated by the standard deviation of these individual velocity vectors within the 1° latitude bins. The figure shows that the winds in UV1 are slower than those in CB2 except near zero latitude. The differences between the UV1 zonal winds and the CB2 zonal winds, which are displayed in Figure 6, further suggest that relatively large differences are concentrated in the centers of westward and eastward jets. This is consistent with the inference from the thermal wind equation that the winds decay with altitude in the high troposphere of Jupiter [*Gierasch et al.*, 1986; *Flasar et al.*, 2004].

[11] Figure 7 shows a comparison between the average UV1 zonal winds and the results from the CIRS data [*Flasar et al.*, 2004; *Simon-Miller et al.*, 2006]. In Figure 7, the thick and thin lines are the zonal winds at 315 mbar and 499 mbar, respectively, inferred by integrating the thermal wind equation. The integration starts with the cloud-tracked wind profile derived from the CB2 filter of Cassini imaging data [*Porco et al.*, 2003], assigning it to the 600-mbar level, and uses the temperatures derived from the Cassini CIRS data to integrate upward [*Flasar et al.*, 2004; *Simon-Miller et al.*, 2006]. The points in Figure 7 are the same as those shown in Figure 5b, and represent the high-altitude zonal wind from the UV1 filter. Figure 7 shows a good match between the UV1 zonal wind and 499-mbar zonal winds from the CIRS data. The match suggests that the UV1 zonal winds probably correspond to a pressure level that is around 499 mbar if we assume the pressure level of CB2 zonal winds is 600 mbar. The 499-

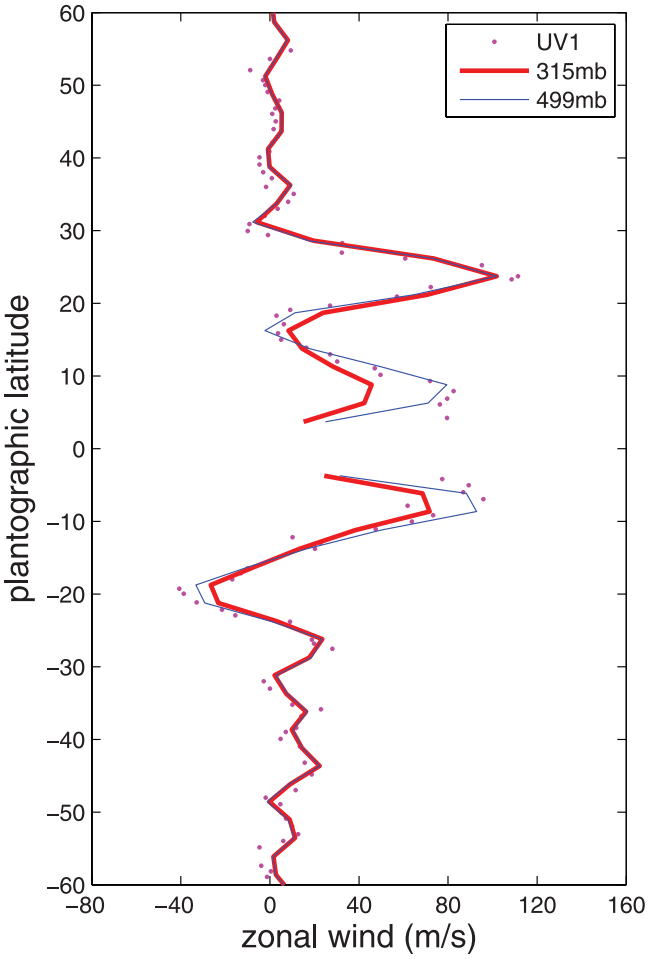

Figure 7. Comparison between the average UV1 zonal winds and the results from the CIRS data. The high-altitude zonal wind profiles at 315 mbar and 499 mbar come from the CIRS data on the assumption that the base zonal winds from CB2 are at 600 mbar [*Flasar et al.*, 2004; *Simon-Miller et al.*, 2006]. Equatorial latitudes between −3° and 3° are omitted in the CIRS profile because the thermal wind equation greatly amplifies the errors in temperature when latitude is small.

mbar pressure level of UV1 zonal wind is reasonable on the basis of the optical characteristics of UV1 filter. The effective pressure level of the UV1 filter with optical depth $\tau = 1$ is 350 mbar (Table 1). It is not much different than 499 mbar, so the contrast from deeper atmosphere (499 mbar) can propagate up to higher level (350 mbar) via scattering. The Pioneer experiences on Venus show that we see through a UV scattering gas and haze down to about $\tau = 2-3$ quite easily [*Del Genio and Rossow*, 1990]. The recent Cassini observations of Titan also verify that we can see the surface in CB3 filter with the optical depth $\tau = 3$ at surface [*Porco et al.*, 2005]. Therefore, if these feature contrasts in UV1 images are produced at 499 mbar, they can still be seen at the top of the atmosphere. At latitudes > 35°N the stratospheric haze has significant opacity, especially in the ultraviolet [*West et al.*, 2004]. This suggests that the UV1 zonal winds correspond to higher altitudes (pressures < 0.5 bar) than the UV1 winds at lower latitudes. Unfortunately, the vertical structure of zonal winds from the CIRS [*Flasar et al.*, 2004; *Simon-Miller et al.*, 2006] does not show obvious vertical changes of zonal winds above 0.5 bar for latitudes > 35°N, so that it is difficult to estimate the pressure level of the UV1 zonal winds at latitudes > 35°N from the CIRS data.

[12] The exact altitude of the UV1 zonal winds depends on the choice of 600 mbar as the level to start the integration of the CIRS data, and that has a large uncertainty. Estimates range from 0.5 bar to 1.0 bar [*Banfield et al.*, 1998; *Irwin et al.*, 2005]. A safer statement is that the features used for cloud tracking in the UV1 are ~0.2 scale heights higher than those used in CB2, which follows because the measured temperature gradient determines the wind shear with respect to log (P), i.e., scale heights. In addition, the resolution of the CIRS data (~2.5° of latitude) and the UV1 average zonal winds in this study (~1° of latitude) are much lower than the resolution of the CB2 zonal wind (~0.1 of latitude), which suggests that the high-altitude zonal winds from this study and the CIRS may have lost some fine structures.

[13] This difference in resolution could account for some of the difference between the UV1 profile and the CB2 profile shown in Figure 5, but it is a small effect. If the zonal velocity profile were a sinusoid with wavelength L, averaging in a box of width h would reduce the apparent amplitude by a factor $\sin x/x$, where $x = \pi h/L$. For $h = 1°$ and $L = 10°$, this factor is 0.98. For $h = 1°$ and $L = 5°$, which is the wavelength at high latitudes, the factor is 0.94. Both of these factors correspond to a small reduction in amplitude compared to the reduction from CB2 to UV1 shown in Figure 5.

[14] Previous measurements of high-altitude zonal winds utilizing the debris of Comet Shoemaker-Levy 9 [*Banfield et al.*, 1996] and using the UV filter at 218 nm [*Vincent et al.*, 2000] also show zonal winds decreasing from the principal cloud deck. In this respect, our UV1 zonal winds are consistent with the previous measurements. However, previous measurements [*Banfield et al.*, 1996; *Vincent et al.*, 2000] refer to higher altitudes (a few tens of millibars) than the estimated pressure level of the UV1 measurement in this study. The higher altitude is where the impact debris of Comet Shoemaker-Levy 9 was deposited [*Banfield et al.*, 1996]. In addition, the UV filter at 218 nm is at a shorter wavelength than Cassini's UV1 filter [*Vincent et al.*, 2000]. The estimation of the pressure level in the previous wind measurements utilized the decay rate of zonal winds at 270 mbar derived by the Voyager IRS data [*Gierasch et al.*, 1986] and assumed the decay rate keeps constant through the upper troposphere to stratosphere [*Banfield et al.*, 1996; *Vincent et al.*, 2000]. The CIRS data generates a zonal wind profile in a wide altitude range (600 mbar to less than 1 mbar) [*Flasar et al.*, 2004] so it offers an opportunity to check the pressure level of wind measurements in the previous studies.

[15] The thermal wind equation does not hold at the equator, so we estimate the vertical change of the zonal wind at the equator by extrapolating the thermal winds at ±3° latitudes. The extrapolation for both 315 mbar and 499 mbar (Figure 7) suggests that the vertical shear of zonal winds near the equator would have the same sign as the thermal wind shear at ±3° latitude, which has winds

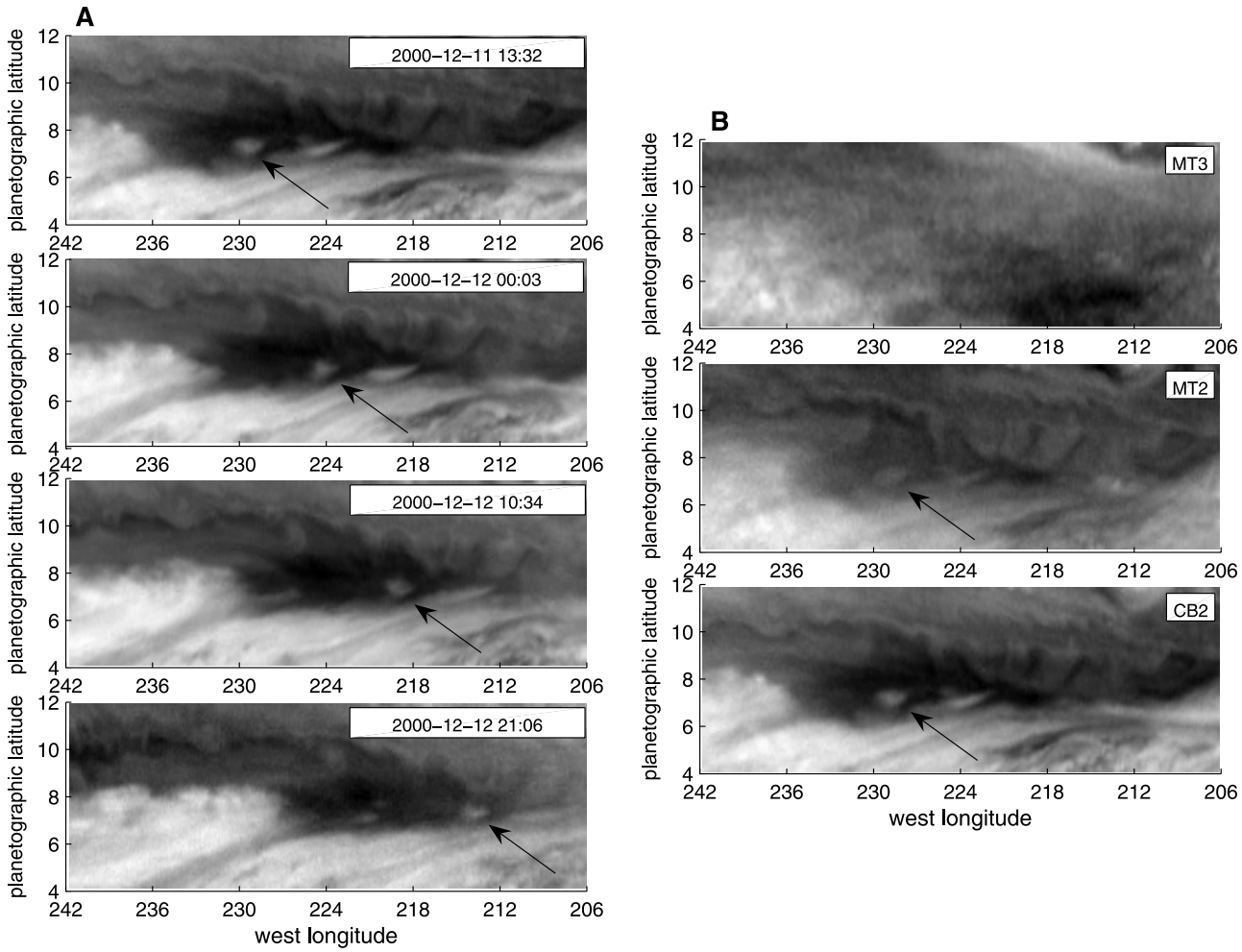

Figure 8. Time series of a deep cloud through a hot spot. (a) Time series of CB2 images separated by 10.5 hours. (b) Multifilter images corresponding to the top panel of Figure 8a. The MT3, MT2, CB2 images of Figure 8b are near-simultaneous images separated by 40 s. The mean value of every constant-latitude line in MT3 images is removed so that these feature contrasts covered by the equatorial haze of MT3 can be seen.

decreasing with altitude. However, Figure 5b shows that the UV1 zonal winds are not less than the CB2 zonal winds within ±3° of the equator, which means that zonal winds do not decrease with altitude. The different sense of vertical shear of zonal winds near the equator probably offers some clues to the mechanisms of prograde equatorial jets on the giant planets, and is worthy of further study.

4. Low-Altitude Winds

[16] The information on deep winds is relatively scarce compared to that on high-altitude winds because of obscuration from over-lying clouds. The DWE on the Galileo probe measured the deep zonal wind profiles to the 21-bar pressure level [*Atkinson et al.*, 1998], but this measurement was limited to a single site at 7.4°N. The probe entered one of Jupiter's 5-μm hot spots, where a hole 5000 km wide exists in the visible top clouds. Fortunately, some deeper clouds are detected through the hot spots in the Cassini ISS high-quality images. The motions of these deeper clouds make it possible to directly measure the deeper zonal winds below the visible top clouds.

[17] Figure 8a is a time sequence of CB2 images separated by 10.5 hours, in which a cloud feature moves across a hot spot from west to east. The cloud feature has a velocity of 175 m/s, which is much stronger than the corresponding CB2 zonal wind in the visible cloud deck (110 ± 20 m/s at this latitude). The hot spots move at the latter speed. The substantial vertical shear suggested by Figure 8 is consistent with the Galileo DWE and the numerical simulation [*Showman and Dowling*, 2000]. Figure 8b is a multifilter image set corresponding to the top panel of Figure 8a. The MT3, MT2, CB2 images of Figure 8b are near-simultaneous images separated by 40 s. The multifilter images show that the cloud is visible in CB2 and MT2 and invisible in MT3, which suggests that the cloud is not a high-altitude feature. Therefore the cloud pointed to by white arrows in Figure 8 is probably a deeper cloud below the visible cloud deck. There are two kinds of clouds below the principal cloud deck: ammonia hydrosulfide (NH_4SH) with cloud base ~2 bars and water (H_2O) with cloud base ~6 bars [*Atreya et al.*, 1997]. In addition, the fact that the cloud is visible in MT2 images suggests that the top of the cloud is above the 3-bar level, which is the pressure level of the optical depth $\tau = 1$

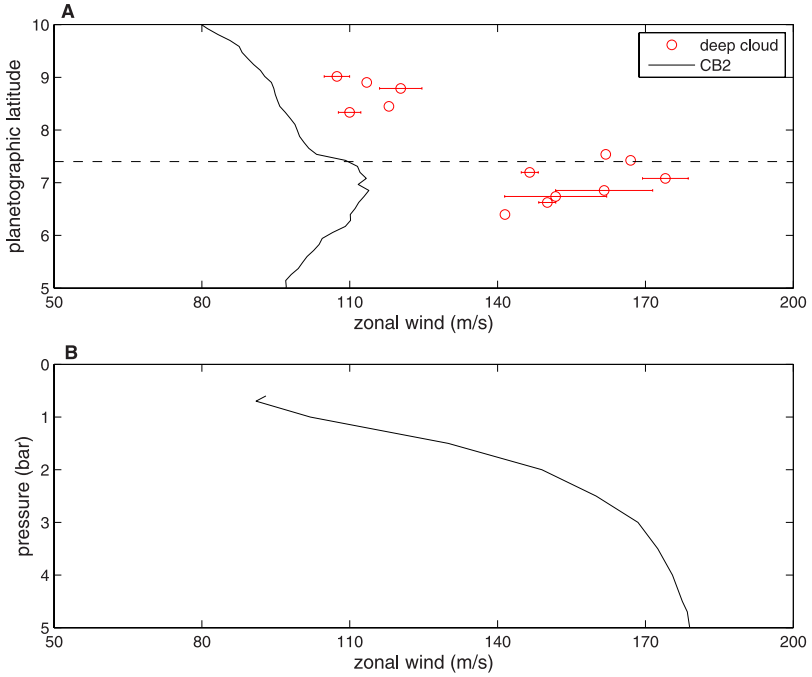

Figure 9. Comparison between the zonal winds by tracking features through hot spots, the zonal winds for all features in CB2 images, and the deep zonal winds from the Galileo probe [*Atkinson et al.*, 1998]. Each red circle without an error bar is the velocity of a deep feature that only can be tracked in a pair of images. Each red circle with an error bar is the velocity of a deep feature that is tracked in more than one pair of images, or the velocity of multiple measurements on different features at the same latitude. Error bars are calculated by the standard deviation of the multiple measurements at the same latitude. The CB2 zonal wind profile between latitudes 5°N and 10°N is the same as the $CB2_a$ zonal wind in Figure 5 [*Porco et al.*, 2003]. (a) Dashed line represents the latitude of Galileo probe. (b) Results of the DWE on the Galileo probe [*Atkinson et al.*, 1998].

for the MT2 filter [*West et al.*, 2004]. Model simulations [*Del Genio and McGrattan*, 1990; *Hueso and Sanchez-Lavega*, 2001] suggest that strong moist convection, originated at the pressure level $\sim$ 5 bars, can extend above the 0.5-bar pressure level on Jupiter. The moist convective storm appearing in four-filter maps of Figure 3 also shows that some convective storms have large vertical extent. On the basis of these factors, the features within hot spots could be either ammonium hydrosulfide clouds, whose cloud base is $\sim$2 bars or water clouds that extend above 3 bars.

[18] The previous wind measurements in the regions of hot spots [*Hueso and Sanchez-Lavega*, 1998; *Vasavada et al.*, 1998] mainly tracked features around the hot spots. In this study, these features we tracked are different from these features measured in the previous two papers [*Hueso and Sanchez-Lavega*, 1998; *Vasavada et al.*, 1998]. They move across the centers of hot spots and have faster zonal wind than the zonal winds at the principal cloud deck, which suggests that these features moving across the hot spots probably are deep clouds and are mainly controlled by the deep faster ambient zonal wind.

[19] Figure 9 shows the measurements of deep zonal winds by tracking these cloud features observed within hot spots and comparison with the results of Galileo DWE. In total, 15 cloud features sitting at 13 different latitudes of the equatorial regions of Jupiter are tracked in this study. Our deep zonal winds at different latitudes (from latitude 6°N to 9°N) extend the results of Galileo DWE, and are consistent with the theoretical and numerical results of deep convection models, which say that the strong equatorial prograde jets of the giant planets penetrate to deep levels [*Busse*, 1976; *Sun et al.*, 1993; *Christensen*, 2001; *Aurnou and Olson*, 2001; *Yano et al.*, 2003]. The velocity that we measure at the latitude of the Galileo probe (7.4°N planetographic) is around 170 m/s, which is equal to the zonal wind at the 3-bar pressure level determined by the Galileo probe (bottom panel of Figure 8) [*Atkinson et al.*, 1998]. If the Galileo probe results in 1995 can be applied to the Cassini flyby in 2000, the ammonium hydrosulfide (NH_4SH) cloud can be ruled out as a candidate for the deeper clouds detected through hot spots because the temperature at the 3-bar level is too high for ammonium hydrosulfide to condense. Therefore the cloud features detected through hot spots are probably thick water clouds extending above 3 bars.

5. Conclusions

[20] High-quality images from the Cassini ISS, acquired in nine filters, are used to measure the high-altitude and low-altitude zonal winds of Jupiter. The first systematic measurements of the high-altitude zonal winds by tracking these small features unique to UV1 images certify that the winds are weaker at the higher altitudes. Winds at the lower altitudes are measured by tracking cloud features through hot spots. The deep zonal winds are consistent with the results from the Galileo probe, provided the clouds are at a

pressure level around 3 bars. These new results will shed light on the dynamics of the Jovian atmosphere and the internal structure of Jupiter.

[21] **Acknowledgments.** We thank Ulyana Dyudina and Colette Salyk for their helpful suggestions on the technical aspects of this article. Cassini project funds supported this research.

References

Atkinson, D. H., J. B. Pollack, and A. Seiff (1998), The Galileo Probe Doppler Wind Experiment: Measurement of the deep zonal winds on Jupiter, *J. Geophys. Res.*, *103*(E10), 22,911–22,928.

Atreya, S. K., M. H. Wong, T. C. Owen, H. B. Niemann, and P. R. Mahaffy (1997), Chemistry and clouds of the Jupiter's atmosphere: A Galileo perspective, in *The Three Galileos: The Man, the Spacecraft, the Telescope*, edited by C. Barbieri et al., p. 249, Springer, New York.

Aurnou, J. M., and P. L. Olson (2001), Strong zonal winds from thermal convection in a rotating spherical shell, *Geophys. Res. Lett.*, *28*(13), 2557–2559.

Banfield, D., P. J. Gierasch, S. W. Squyres, P. D. Nicholson, B. J. Conrath, and K. Matthews (1996), 2 μm spectrophotometry of Jovian stratospheric aerosols—Scattering opacities, vertical distributions, and wind speeds, *Icarus*, *121*, 389–410.

Banfield, D., P. J. Gierasch, M. Bell, E. Ustinov, A. P. Ingersoll, A. R. Vasavada, R. A. West, and M. J. S. Belton (1998), Jupiter's cloud structure from Galileo imaging data, *Icarus*, *135*, 230–250.

Barcilon, A., and P. Gierasch (1970), A moist, Hadley cell model for Jupiter's cloud bands, *J. Atmos. Sci.*, *27*(4), 550–560.

Busse, F. H. (1976), Simple model of convection in Jovian atmosphere, *Icarus*, *29*, 255–260.

Christensen, U. R. (2001), Zonal flow driven by deep convection in the major planets, *Geophys. Res. Lett.*, *28*(13), 2553–2556.

Del Genio, A. D., and K. B. McGrattan (1990), Moist convection and the vertical structure and water abundance of Jupiter's atmosphere, *Icarus*, *84*, 29–53.

Del Genio, A. D., and W. B. Rossow (1990), Planetary-scale waves and the cyclic nature of cloud top dynamics on Venus, *J. Atmos. Sci.*, *47*(3), 293–318.

Flasar, F. M., et al. (2004), An intense stratospheric jet on Jupiter, *Nature*, *427*(6970), 132–135.

Garcia-Melendo, E., and A. Sanchez-Lavega (2001), A study of the stability of Jovian zonal winds from HST images: 1995–2000, *Icarus*, *152*, 316–330.

Gierasch, P. J. (1976), Jovian meteorology—Large-scale moist convection, *Icarus*, *29*, 445–454.

Gierasch, P. J., B. J. Conrath, and J. A. Magalhaes (1986), Zonal mean properties of Jupiter upper troposphere from Voyager infrared observations, *Icarus*, *67*, 456–483.

Hueso, R., and A. Sanchez-Lavega (1998), Motions in Jovian hot spot-plume regions using Voyager images, *Icarus*, *136*, 353–357.

Hueso, R., and A. Sanchez-Lavega (2001), A three-dimensional model of moist convection for the giant planets: The Jupiter case, *Icarus*, *151*, 257–274.

Ingersoll, A. P., and D. Pollard (1982), Motion in the interiors and atmospheres of Jupiter and Saturn—Scale analysis, anelastic equations, barotropic stability-criterion, *Icarus*, *52*, 62–80.

Ingersoll, A. P., R. F. Beebe, S. A. Collins, G. E. Hunt, J. L. Mitchell, P. Muller, B. A. Smith, and R. J. Terrile (1979), Zonal velocity and texture in the Jovian atmosphere inferred from Voyager images, *Nature*, *280*(5725), 773–775.

Ingersoll, A. P., R. F. Beebe, J. L. Mitchell, G. W. Garneau, G. M. Yagi, and J. P. Muller (1981), Interaction of eddies and mean zonal flow on Jupiter as inferred from Voyager-1 and Voyager-2 images, *J. Geophys. Res.*, *86*(A10), 8733–8743.

Irwin, P. G. J., K. Sihra, N. Bowles, F. W. Taylor, and S. B. Calcutt (2005), Methane absorption in the atmosphere of Jupiter from 1800 to 9500 cm^{-1} and implications for vertical cloud structure, *Icarus*, *176*, 255–271.

Li, L., A. P. Ingersoll, A. R. Vasavada, C. C. Porco, A. D. Del Genio, and S. P. Ewald (2004), Life cycles of spots on Jupiter from Cassini images, *Icarus*, *172*, 9–23.

Limaye, S. S. (1986), Jupiter—New estimates of the mean zonal flow at the cloud level, *Icarus*, *65*, 335–352.

Limaye, S. S. (1989), Jupiter: Short-term variations of the mean zonal flow at the cloud level, in *Time-Variable Phenomena in the Jovian System*, edited by M. J. S. Belton, R. A. West, and J. Rahe, *NASA Spec. Publ.*, *494*, 311–323.

Limaye, S. S., H. E. Revercomb, L. A. Sromovsky, R. J. Krauss, D. A. Santek, V. E. Suomi, S. A. Collins, and C. C. Avis (1982), Jovian winds from Voyager-2: 1. Zonal mean circulation, *J Atmos. Sci.*, *39*(7), 1413–1432.

Porco, C. C., et al. (2003), Cassini imaging of Jupiter's atmosphere, satellites, and rings, *Science*, *299*, 1541–1547.

Porco, C. C., et al. (2004), Cassini imaging science: Instrument characteristics and anticipated scientific investigations at Saturn, *Space Sci. Rev.*, *115*(1–4), 363–497.

Porco, C. C., et al. (2005), Imaging of Titan from the Cassini spacecraft, *Nature*, *434*(7030), 159–168.

Riddle, A. C., and J. W. Warwick (1976), Redefinition of system-3 longitude, *Icarus*, *27*, 457–459.

Rogers, J. H. (1995), *The Giant Planet Jupiter*, Cambridge Univ. Press, New York.

Showman, A. P., and T. E. Dowling (2000), Nonlinear simulations of Jupiter's 5-micron hot spots, *Science*, *289*, 1737–1740.

Simon, A. A. (1999), The structure and temporal stability of Jupiter's zonal winds: A study of the north tropical region, *Icarus*, *141*, 29–39.

Simon-Miller, A. A., B. J. Conrath, P. J. Gierasch, G. S. Orton, R. K. Achterberg, F. M. Flasar, and B. M. Fischer (2006), Jupiter's atmospheric temperatures: From Voyager IRIS to Cassini CIRS, *Icarus*, *180*, 98–112.

Smith, B. A. (1976), Motion and morphology of clouds in the atmosphere of Jupiter, in *Jupiter*, edited by T. Gehrels, pp. 564–618, Univ. of Ariz. Press, Tucson.

Sun, Z. P., G. Schubert, and G. A. Glatzmaier (1993), Banded surface flow maintained by convection in a model of the rapidly rotating giant planets, *Science*, *260*, 661–664.

Vasavada, A. R., et al. (1998), Galileo imaging of Jupiter's atmosphere: The Great Red Spot, equatorial region, and White Ovals, *Icarus*, *135*, 265–275.

Vincent, M. B., et al. (2000), Jupiter's polar regions in the ultraviolet as imaged by HST/WFPC2: Auroral-aligned features and zonal motions, *Icarus*, *143*, 205–222.

West, R. A., K. H. Baines, A. J. Friedson, D. Banfield, B. Ragent, and F. W. Taylor (2004), *Jupiter: The Planet, Satellites and Magnetosphere*, *Cambridge Planet. Sci. Ser.*, edited by F. Bagenal et al., Cambridge Univ. Press, New York.

Yano, J. I., O. Talagrand, and P. Drossart (2003), Outer planets: Origins of atmospheric zonal winds, *Nature*, *421*(6918), 36.

Young, R. E. (2003), The Galileo probe: How it has changed our understanding of Jupiter, *New Astron. Rev.*, *47*, 1–51.

A. D. Del Genio, NASA Goddard Institute for Space Studies, New York, NY, USA. (delgenio@giss.nasa.gov)

S. P. Ewald, A. P. Ingersoll, and L. Li, Division of Geological and Planetary Sciences, California Institute of Technology, MS 150-21, Pasadena, CA 91125, USA. (spe@gps.caltech.edu; api@gps.caltech.edu; liming@gps.caltech.edu)

C. C. Porco, CICLOPS/Space Science Institute, Boulder, CO, USA. (carolyn@ciclops.org)

A. A. Simon-Miller, NASA Goddard Space Flight Center, Greenbelt, MD, USA. (simon@lepasm.gsfc.nasa.gov)

A. R. Vasavada and R. A. West, Jet Propulsion Laboratory, California Institute of Technology, Pasadena, CA, USA. (ashwin.r.vasavada@jpl.nasa.gov; robert.a.west@jpl.nasa.gov)